Multimode metal-insulator-metal waveguides: Analysis and experimental characterization

Chien-I Lin and Thomas K. Gaylord[*]

School of Electrical and Computer Engineering, Georgia Institute of Technology, Atlanta, Georgia 30332-0250, USA
(Received 3 December 2011; published 3 February 2012)

The analysis and experimental characterization of the propagation constants and attenuation coefficients of surface plasmon (SP) modes in planar multimode metal-insulator-metal (MIM) waveguides are presented. The experimental characterization is based on determining the width of the reflection angular spectrum in the attenuated total reflection (ATR) configuration. Due to its transverse character, the ATR configuration provides a more straightforward and simpler way to determine the propagation constants and attenuation coefficients of plasmonic modes in MIM structures, compared to using tapered end-couplers with multiple waveguide samples or near-field scanning optical microscopy (NSOM). In this paper, the propagation constants and attenuation coefficients of multimode MIM structures are investigated, and MIM waveguide structures with 730 and 1460 nm SiO$_2$ cores and Au claddings are fabricated and experimentally characterized. The measurement results indicate that the absorption of Au is responsible for the high attenuation in MIM plasmonic modes, while scattering loss is another source of attenuation for higher-order modes (smaller zigzag angles). To the best of the authors' knowledge, the present work represents the first time the attenuation coefficient and propagation constant of each mode in a multimode MIM waveguide have been individually measured.

I. INTRODUCTION

Metal-insulator-metal (MIM) waveguides with subwavelength apertures are of great interest in plasmonics,[1–4] primarily for their potential in realizing integrated optical nanocircuitry. However, large-core MIM waveguides may also be used for lower-loss interconnects in surface plasmon (SP)-based optical nanocircuitry. Therefore it is important to understand the propagation properties in large-core MIM waveguides, which, similar to conventional dielectric optical waveguides, support more than one mode. In conventional experimental characterization techniques,[5–8] all the waveguide modes are excited simultaneously; therefore the propagation constant and attenuation coefficient of each mode cannot be easily extracted from the measurement data. In the present work, by using an attenuated total reflection (ATR) configuration, the propagation constants and attenuation coefficients of the waveguide modes in multimode MIM waveguides have been experimentally measured. The ATR configuration is highly angularly selective; therefore each mode can be separately excited and characterized. Two MIM (Au-SiO$_2$-Au) structures with 730 and 1460 nm oxide cores have been fabricated and characterized at $\lambda = 1550$ nm.

II. MIM MODE ANALYSIS

Figure 1 shows the schematic diagram of an MIM structure. By using the boundary conditions for TM waves in the MIM structure, the characteristic equations are given as

$$\tanh\left(\frac{\kappa_i d_i}{2}\right) = -\frac{\kappa_m}{\kappa_i}\frac{\varepsilon_i}{\varepsilon_m} \qquad (1)$$

for even TM modes and

$$\tanh\left(\frac{\kappa_i d_i}{2}\right) = -\frac{\kappa_i}{\kappa_m}\frac{\varepsilon_m}{\varepsilon_i} \qquad (2)$$

for odd TM modes,[9,10] where $\kappa \equiv (k_z^2 - k_0^2\varepsilon)^{1/2}$ are the complex wave vectors in the x direction, with k_z being the wave vector in the z direction and k_0 being the free-space wave vector. In the case that both ε_i and ε_m are real, a real κ_i indicates that the wave is evanescent in the insulator core and that the mode is a plasmonic mode, and an imaginary κ_i indicates that the wave is sinusoidal in the insulator core and that the mode is referred to as an oscillatory mode throughout the paper. The latter is similar to a regular dielectric optical waveguide mode. A k_z value that satisfies Eqs. (1) or (2) is the complex propagation constant $\gamma = \beta - j\alpha$ corresponding to a TM mode, where β is the propagation constant and α is the attenuation coefficient.

Figure 2 shows the effective mode indices $N \equiv \beta/k_0$ and propagation lengths $L \equiv 1/(2|\alpha|)$ as functions of dielectric core thickness d_i for TM modes in an MIM (Au-SiO$_2$-Au) waveguide at $\lambda = 1550$ nm. At this wavelength, Au has a dielectric constant $\widetilde{\varepsilon}_{Au} = -115 - j11.3$.[11] The dielectric constant for the SiO$_2$ core is assumed to be $\varepsilon_i = (1.4877)^2$. It can be observed from Fig. 2(a) that at small core thicknesses d_i, only the fundamental mode TM$_0$ exists. As d_i increases, the MIM waveguide starts to support higher-order modes, and the cutoff thickness is larger for higher-order modes. The modes with effective mode indices higher than the refractive index of the insulator are plasmonic modes, and the others are oscillatory waveguide modes. The TM$_0$ mode is plasmonic for any core thickness. The TM$_1$ mode is an oscillatory mode at smaller core thickness but becomes a plasmonic mode at larger thickness. The higher-order modes, such as the TM$_2$ and TM$_3$ modes, are oscillatory modes for any core thickness. Figure 2(b) shows that the propagation lengths are larger for larger core thicknesses for TM$_0$ to TM$_3$ modes. From Fig. 2, the two plasmonic modes, TM$_0$ and TM$_1$ at large core thickness, become practically degenerate at large d_i, because the two Au/SiO$_2$ interfaces become decoupled and the TM$_0$ and TM$_1$ modes propagate like independent SP modes at the Au/SiO$_2$
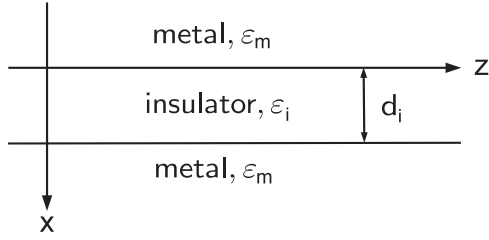
FIG. 1. Configuration and coordinate system of a metal-insulator-metal (MIM) structure. The structure is invariant in the y direction.

interfaces. This can be observed from both values of N and L of the TM_0 and TM_1 modes, which approach the values of N_{eff} and L of the SP mode at a single Au/SiO$_2$ interface, respectively. On the other hand, the higher-order modes, TM_2 and TM_3 modes, do not approach the SP mode at Au/SiO$_2$ interfaces. As d_i increases, the attenuations of the oscillatory modes always decrease. This property is also observed for the modes in lossy dielectric optical waveguides.[12] It is worth mentioning that at larger d_i values, the attenuation of the fundamental mode exceeds the attenuation of the oscillatory modes (e.g., TM_2 and TM_3 modes). This differs from conventional dielectric waveguides, in which the fundamental mode always has the lowest attenuation. For data transmission purposes, it is favorable that the fundamental mode has dominantly low attenuation. Therefore, when other modes which have comparable attenuation exist, it is critical to investigate the propagation constant and attenuation coefficient of each mode.

Similar analysis can be preformed for TE modes in the MIM structure. The characteristic equations for the TE modes are given as

$$\tan\left(\frac{k_i d_i}{2}\right) = \frac{\kappa_m}{k_i} \tag{3}$$

for even TE modes and

$$\tan\left(\frac{k_i d_i}{2}\right) = -\frac{k_i}{\kappa_m} \tag{4}$$

for odd TE modes,[9,10] where $k_i \equiv (k_0^2 \varepsilon - k_z^2)^{1/2} = -j\kappa_i$ is the wave vector in the x direction in the insulator. Unlike the TM modes, the k_i value is always real for a TE mode, and it indicates that the wave is sinusoidal in the insulator core. As a result, the TE modes in MIM structures are oscillatory modes, which are similar to the TE modes in dielectric optical waveguides.

Figure 3 shows the effective mode indices N and propagation lengths L as functions of dielectric core thickness d_i for TE modes in an MIM (Au-SiO$_2$-Au) waveguide at $\lambda = 1550$ nm. At small d_i, no TE mode exists, and the cutoff thickness is larger for higher-order TE modes. Moreover, all the TE modes are below the light line and are similar to dielectric optical waveguide modes. Figure 3(b) shows that the propagation lengths are larger for larger d_i for each mode, and at a given d_i, the propagation lengths are larger for lower-order modes. This phenomenon is similar in lossy dielectric optical waveguides.[12] It is also worth mentioning that, at larger d_i, the TE modes
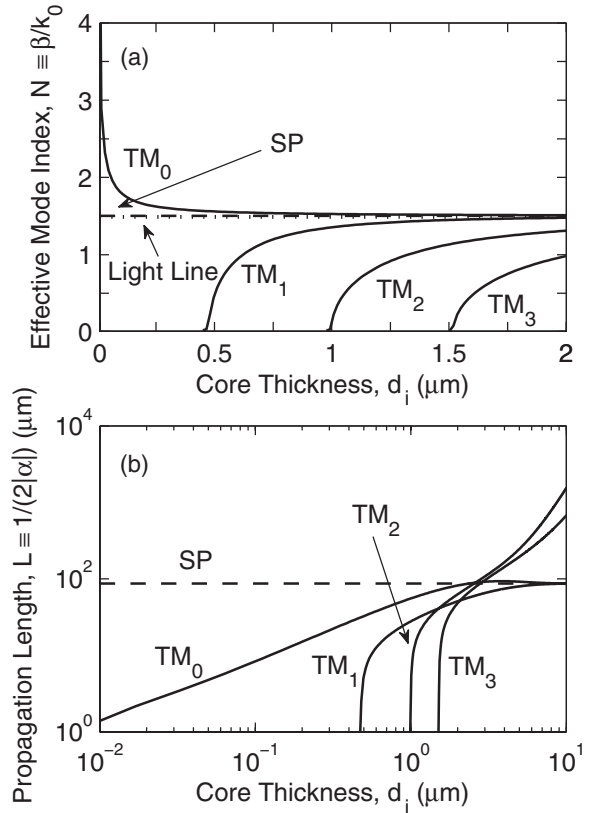

FIG. 2. (a) Effective mode indices $N \equiv \beta/k_0$ and (b) propagation lengths $L \equiv 1/(2|\alpha|)$ for the TM_{0-3} modes as functions of the dielectric core thickness d_i in MIM (Au-SiO$_2$-Au) waveguides at $\lambda = 1550$ nm. The curves for the MIM TM_{0-3} modes and the single Au/SiO$_2$ interface are labeled TM_{0-3} and SP, respectively. The effective mode index for the latter is 1.502 0. The light line in (a) represents light propagation in bulk SiO$_2$, with an effective mode index = 1.487 7.

propagate for a much longer distance than the fundamental plasmonic mode TM_0 does.

III. TRANSVERSE TRANSMISSION/REFLECTION METHOD

The measurement approach presented here is based on the concept of the transverse transmission/reflection (TTR) method,[13–15] which significantly simplifies the loss measurement of the MIM plasmonic modes. The TTR method differs from previous loss measurement methods for MIM waveguides.[5–8] Instead of injecting light through the end of a waveguide,[5–7] the TTR method excites a plasmonic mode from the transverse direction. This can be realized by making one of the metal claddings sufficiently thin (e.g., 3–4 skin depths) for light coupling.[8,15] A high-index prism is then added adjacent to the thin metal layer to enable coupling, as shown in Fig. 4(a).

Based on the transmission matrix formulation,[16] each layer can be represented by a transmission matrix:

$$M_i = \frac{1}{2}\begin{pmatrix} \left(1 + f_i\frac{\kappa_{x,i}}{\kappa_{x,i+1}}\right)\exp(-\kappa_{x,i}d_i) & \left(1 - f_i\frac{\kappa_{x,i}}{\kappa_{x,i+1}}\right)\exp(\kappa_{x,i}d_i) \\ \left(1 - f_i\frac{\kappa_{x,i}}{\kappa_{x,i+1}}\right)\exp(-\kappa_{x,i}d_i) & \left(1 + f_i\frac{\kappa_{x,i}}{\kappa_{x,i+1}}\right)\exp(\kappa_{x,i}d_i) \end{pmatrix} \quad \text{for} \quad i = 0,1,2,3, \tag{5}$$

where for TE waves $f_i = 1$, while for TM waves $f_i = \varepsilon_{i+1}/\varepsilon_i$, and d_i is the thickness of the ith layer. The field amplitudes at each boundary can then be related via the matrix equation

$$\begin{pmatrix} A_4 \\ B_4 \end{pmatrix} = M_3 M_2 M_1 M_0 \begin{pmatrix} A_0 \\ B_0 \end{pmatrix} = M\begin{pmatrix} A_0 \\ B_0 \end{pmatrix}, \tag{6}$$

where A and B are field amplitudes (E_y field for TE wave or H_y field for TM wave) corresponding to $+x$ and $-x$ propagating waves at each interface. The range that each matrix represents is shown in Fig. 4(a). The field amplitudes at the other interfaces can be obtained in a similar manner. Alternatively, the transmission matrix for the prism-loaded MIM can be expressed by

$$M = \begin{pmatrix} m_{11} & m_{12} \\ m_{21} & m_{22} \end{pmatrix}_{\text{MIM}} \begin{pmatrix} \exp(-\kappa_m d_m) & 0 \\ 0 & \exp(\kappa_m d_m) \end{pmatrix}$$
$$\times \begin{pmatrix} m'_{11} & m'_{12} \\ m'_{21} & m'_{22} \end{pmatrix}_{\text{Otto}}, \tag{7}$$

where the subscripts MIM and Otto denote the matrices for structures in Figs. 4(c) and 4(b), respectively. For the MIM structure, $m_{22} = 0$ corresponds to waveguide modes. The reflection coefficient for the prism-loaded MIM structure is

$$r = -\frac{M(2,1)}{M(2,2)}$$
$$\simeq -\frac{m'_{21}}{m'_{22}}\left[1 + \frac{m_{21}}{m_{22}}\frac{m'_{11}m'_{22} - m'_{12}m'_{21}}{m'_{22}m'_{21}}\exp(-2\kappa_m d_m)\right]. \tag{8}$$

Because $m_{22} = 0$ corresponds to MIM modes, m_{22} can be approximated by $k_z - \gamma$ when k_z is close to β, where $\gamma \equiv \beta - \alpha$ is the complex propagation constant of the MIM mode. Therefore Eq. (8) can be further approximated by

$$r \simeq r_{\text{Otto}}\left[1 + \frac{s(k_z)}{k_z - \gamma}\exp(-2\kappa_m d_m)\right], \tag{9}$$

where $r_{\text{Otto}} = -m'_{21}/m'_{22}$ is the reflection coefficient for the Otto configuration in Fig. 4(b), and $s(k_z)$ is a composite function which varies relatively slowly in a small range of k_z. Therefore the fractional reflected power $R = |r|^2$ can be approximated by

$$R \simeq R_{\text{Otto}}\left[1 - \frac{S(k_z)}{(k_z - \beta)^2 + \alpha^2}\exp(-2\kappa_m d_m)\right], \tag{10}$$
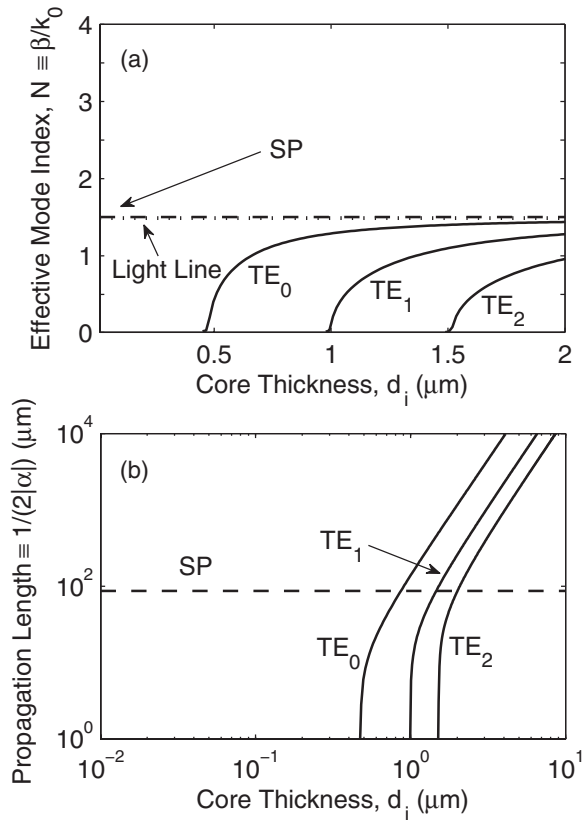

FIG. 3. (a) Effective mode indices N and (b) propagation lengths L for the TE$_{0-2}$ modes as functions of d_i in MIM (Au-SiO$_2$-Au) waveguides at $\lambda = 1550$ nm. The curves for the MIM TE$_{0-2}$ modes and the single Au/SiO$_2$ interface are labeled TE$_{0-2}$ and SP, respectively.
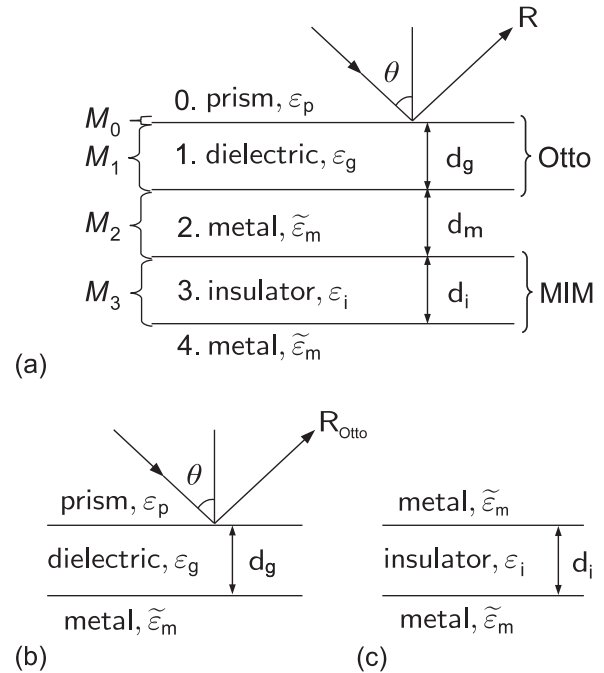

FIG. 4. (a) Schematic diagram of the ATR configuration applied to a symmetric MIM structure. The transmission matrix corresponding to each numbered layer is labeled. (b) A single metal/dielectric interface (Otto configuration, Ref. 17). (c) A symmetric MIM structure.

where $S(k_z)$ is a slowly varying function of k_z. It is shown in Ref. 12 that the approximation in Eq. (10) is valid for metals with smaller absorption loss, such as Au and Ag. Equation (10) shows that R is similar to R_{Otto}, but the former has one or more resonances corresponding to the MIM plasmonic modes near $k_z = \beta$. Equation (10) also indicates that R/R_{Otto} has a Lorentzian-type resonance centered at $N \equiv \beta/k_0$ and a half-width at half minimum (HWHM) $= \alpha/k_0$. It is shown in Refs. 12 and 13 that R/R_{Otto} can be obtained by simply subtracting out the background variation (i.e., R_{Otto}) from R. Therefore, the TTR method provides a straightforward and simple approach for determining the complex propagation constants by using a configuration similar to the prism coupler introduced by Ulrich and Tien[18,19] and to the ATR configuration.[20–22] These experiments characterize the plasmonic modes in a multimode MIM structure, and the attenuation coefficient and the propagation constant of each mode in a multimode MIM waveguide are individually measured.

IV. EXPERIMENTAL CHARACTERIZATION

Using the Metricon model 2010 prism coupler,[23] the TTR method was experimentally applied to two MIM (Au-SiO₂-Au) waveguide structures. The schematic diagram of the experimental configuration is shown in Fig. 5. The coupling head is used to push the MIM structure toward the prism to create a coupling spot where the prism and the MIM structure have intimate contact for light coupling. The force is controlled by air pressure P_c, which is adjustable from 10 to 50 lbs/in². A laser beam is manually adjusted to be centered on the coupling spot for a stronger coupling between the prism and the MIM structures. Two MIM structures with different SiO₂ core thicknesses, $d_i = 730$ and 1460 nm, were fabricated and characterized at $\lambda = 1550$ nm. To ensure the appropriate coupling strength, the Au layer on the top of the structure is 75 nm thick, which is about three skin depths. The Au layer substrate is 400 nm in thickness, which, for practical purposes, is optically semi-infinite. The Au cladding layers
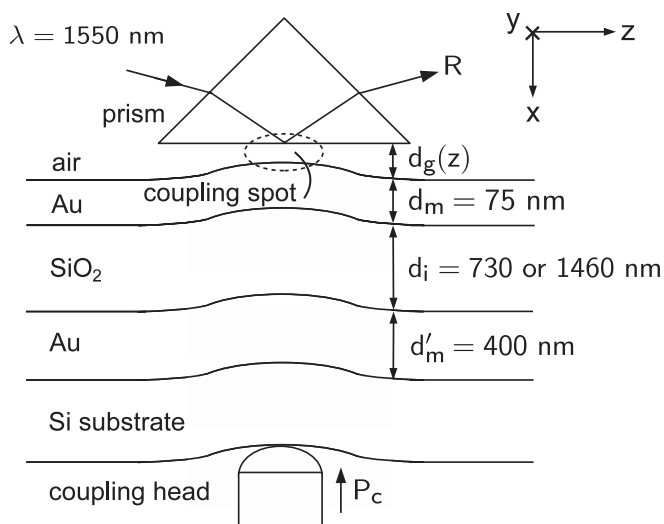

FIG. 5. Schematic diagram of the ATR configuration applied to the MIM structures.

TABLE I. Normalized propagation constants β/k_0 and attenuation coefficients α/k_0 obtained from rigorous calculations for unperturbed MIM structures.

Structure	Mode	β/k_0	α/k_0
$d_i = 730$ nm	TM₀	1.5392	0.002 81
	TM₁	1.1764	0.006 68
	TE₀	1.1020	0.002 56
$d_i = 1460$ nm	TM₀	1.4964	0.001 72
	TM₁	1.4240	0.003 05
	TM₂	1.0801	0.003 20
	TE₀	1.3748	0.000 28
	TE₁	1.0464	0.001 48

were deposited by using an e-beam evaporator at a rate of 0.5 Å/s, with a chamber pressure $\sim 10^{-6}$ Torr. The SiO₂ cores were deposited by using plasma-enhanced chemical vapor deposition (PECVD) at 250 °C, 900 mTorr, with 400 sccm SiH₄ (2% in N₂), 900 sccm N₂O, and rf power $= 10$ and 25 W for the samples with $d_i = 730$ and 1460 nm, respectively.

The propagation constant of the MIM waveguide can be rigorously calculated by using the argument principle method (APM).[24] At $\lambda = 1550$ nm, the refractive index of Au is $\tilde{n}_{Au} = 0.526 - j10.74$,[11] and the refractive indices of the PECVD oxide layers are $n_{SiO_2} = 1.4877$ and 1.468 for the samples with $d_i = 730$ and 1460 nm, respectively. The relatively high refractive index of SiO₂ in the former is a result of incomplete oxidation at low rf power.[25,26] The calculated results for the 730- and 1460-nm core MIM structures are summarized in Table I. It should be noted that in these calculations, it is assumed that the MIM structures have symmetric and semi-infinite claddings on both sides.

The measured TM reflectance angular spectra for the structure in Fig. 5 with $d_i = 730$ nm is shown in Fig. 6(a). The x axis is the effective index $N_{eff} \equiv k_z/k_0 = n_p \sin\theta$, where n_p is the refractive index of the prism and θ is the angle of incidence at the prism/air gap interface. At $\lambda = 1550$ nm, $n_p = 1.9349$. By increasing the pressure of the coupling head P_c, the air gap thickness d_g decreases and a series of spectra were measured. The resonances of R at higher and lower effective mode index N_{eff} correspond to the TM₀ and TM₁ modes in the MIM structure, respectively. Figure 6(b) shows the effective mode index $N'_{TM_0} \equiv \beta'_{TM_0}/k_0$, which corresponds to the resonance minima of the TM₀ resonance, as a function of P_c, and the average of the measurements yields $N'_{TM_0} = 1.5333$, with a standard deviation $\sigma_\beta = 0.0001$. The prime denotes results obtained from the measurements, in contrast to the rigorously calculated results. Figure 6(c) shows the normalized attenuation coefficients $\alpha'_{TM_0}/k_0 =$ HWHMs of the TM₀ mode as a function of P_c, and the average of the measurements yields $\alpha'_{TM_0}/k_0 = 0.002\,47$, with a standard deviation $\sigma_\alpha = 0.000\,07$. This is equivalent to a loss of 0.087 dB/μm or $L = 50\ \mu$m. The resonance minima and HWHMs are obtained after removing the background variation in R; this can be done by leveling both sides of a resonance to unity. It can be observed from Figs. 6(b) and 6(c) that there is no apparent trend in the measured N'_{TM_0} and α'_{TM_0}/k_0 as functions of P_c. The insensitivity of the measurement results to P_c and therefore d_g is important for the
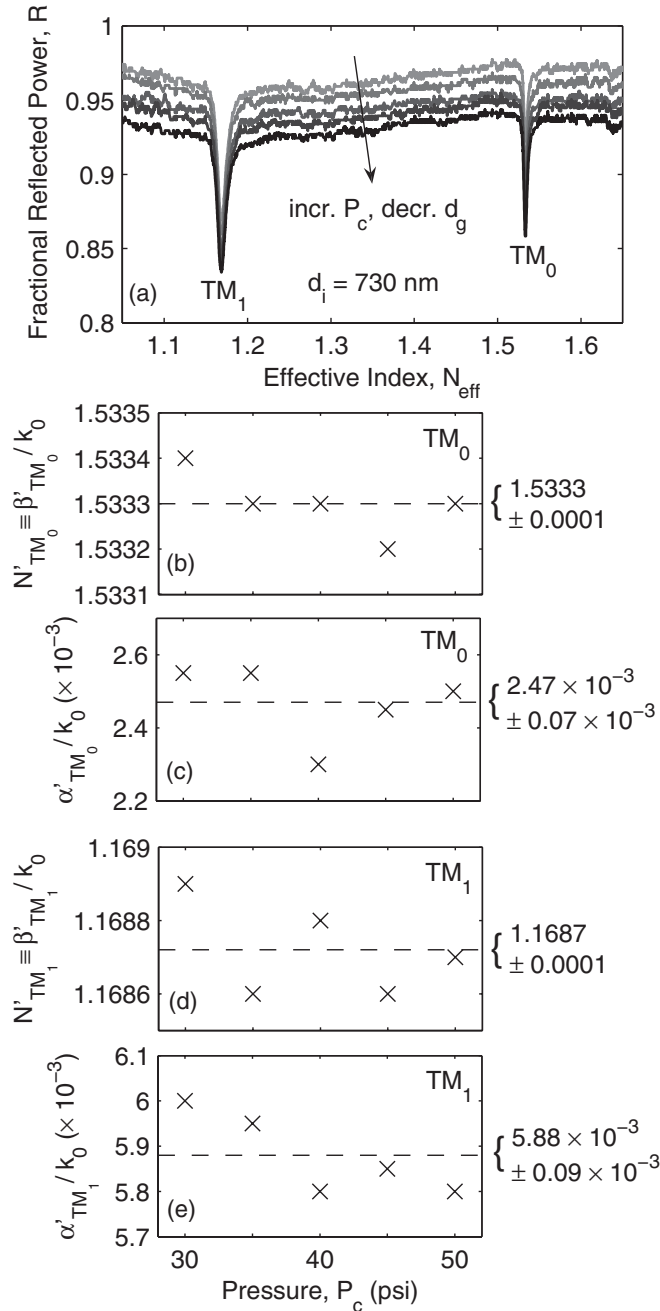
FIG. 6. (a) TM reflectance angular spectra for the structure in Fig. 5 with $d_i = 730$ nm measured at various air gap thicknesses d_g, which correspond to pressures of the coupling head, $P_c = 30, 35, 40, 45$, and 50 psi. (b) The normalized propagation constants $N'_{TM_0} \equiv \beta'_{TM_0}/k_0$ corresponding to the "resonance minima" and (c) the normalized attenuation coefficients $\alpha'_{TM_0}/k_0 =$ HWHMs of the TM_0 resonances at various values of P_c. (d) The normalized propagation constants N'_{TM_1} and (e) the normalized attenuation coefficients α'_{TM_1}/k_0 of the TM_1 resonances at various values of P_c.

application of this approach, because d_g is difficult to quantify experimentally. The experimental results measured at all P_c conditions agree well with the calculated results in both the propagation constant and attenuation coefficient. Similar to the cases of single-mode MIM waveguides,[15] the measured attenuation is about 13% smaller than the calculated value.

The N'_{TM_1} and α'_{TM_1} of the TM_1 mode can also be obtained in the same manner. Figure 6(d) shows N'_{TM_1} as a function of P_c, and the average of the measurements yields $N'_{TM_1} = 1.168\,7$, with a standard deviation $\sigma_\beta = 0.000\,1$. Figure 6(e) shows α'_{TM_1}/k_0 as a function of P_c, and the average of the measurements yields $\alpha'_{TM_1}/k_0 = 0.005\,88$, with a standard deviation $\sigma_\alpha = 0.000\,9$. This is equivalent to a loss of $0.21\text{dB}/\mu\text{m}$ or $L = 21\,\mu\text{m}$. Again, there is no apparent trend in the measured N'_{TM_1} and α'_{TM_1}/k_0 as functions of P_c. The agreement between the experimental results and the calculated result is very good. Similar to the case of the TM_0 mode, the measured attenuation is about 13% smaller than the calculated value.

The measured TE reflectance angular spectra for the same structure is shown in Fig. 7(a). The TE_0 mode has a much weaker resonance strength than the TM modes [Fig. 6(a)], because the portion of penetrated field into the absorptive Au claddings is less in the former. As a result, the coupling between the prism and the TE mode is weaker. The N'_{TE_0} and α'_{TE_0} of the TE_0 mode are also obtained from the resonance minimum and HWHM of the TE_0 resonance in each measurement curve. Figure 7(b) shows N'_{TE_0} as a function of P_c, and the average of the measurements yields $N'_{TE_0} = 1.107\,3$, with a standard deviation $\sigma_\beta = 0.000\,4$. Figure 7(c) shows α'_{TE_0}/k_0 as a function of P_c, and the average of the measurements yields $\alpha'_{TE_0}/k_0 = 0.003\,10$, with a standard deviation $\sigma_\alpha = 0.000\,2$.
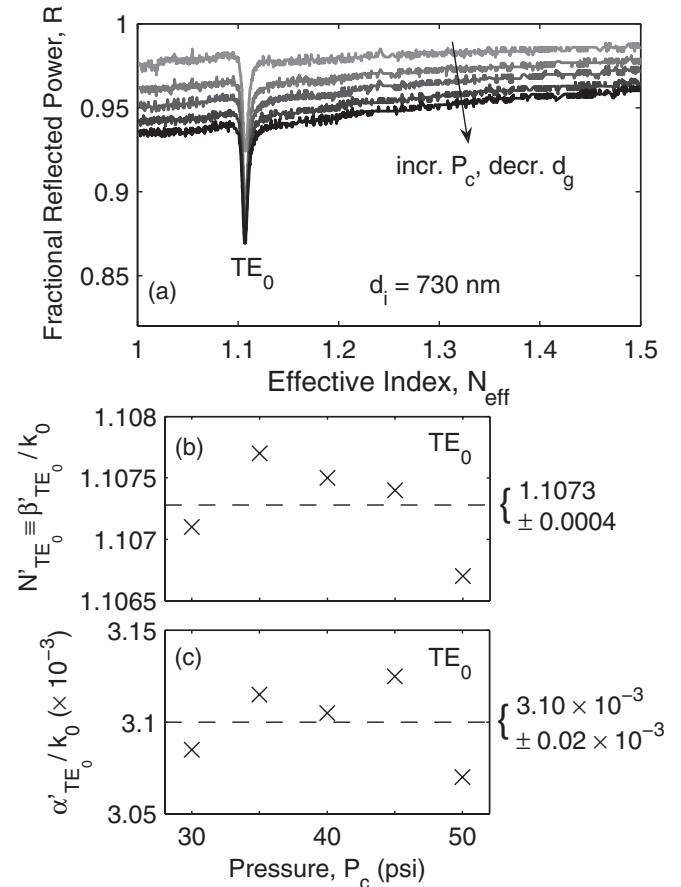

FIG. 7. (a) TE reflectance angular spectra for the structure in Fig. 5 with $d_i = 730$ nm measured at various P_c values. (b) N'_{TE_0} and (c) α'_{TE_0}/k_0 of the TE_0 mode.

This is equivalent to a loss of 0.11dB/μm or $L = 40$ μm. The measured N'_{TE_0} and $\alpha'_{\text{TE}_0}/k_0$ are very self-consistent as P_c varies. Although the experimental results agree with the calculation, unlike the previous two cases, the measured attenuations are larger than the calculated one. This is probably due to loss mechanisms other than the absorption loss of the metal, which is the only loss mechanism taken into account in the calculation. Specifically, scattering loss caused by the rough Au/SiO$_2$ interfaces is a possible source of extra loss associated with the TE$_0$ mode. Scattering loss is much larger for higher-order modes that have smaller zigzag angles in the cores[12] and stronger interaction with the interface. A further discussion of this effect is presented in Sec. V.

For the structure in Fig. 5 with $d_i = 1460$ nm, the measured TM reflectance angular spectra is shown in Fig. 8(a). The three resonances of R correspond to the TM$_0$, TM$_1$, and TM$_2$ modes in the MIM structure. It is shown that the resonances of the TM$_0$ and TM$_1$ modes are much weaker at larger d_g, while the resonance strength of the TM$_2$ mode is approximately independent of d_g. This is because the air gap thickness d_g has only a small effect on the coupling efficiency of a mode with low effective mode index.

Figures 8(b) and 8(c) show the effective mode index N'_{TM_0} and normalized attenuation coefficients $\alpha'_{\text{TM}_0}/k_0$ of the TM$_0$ as functions of P_c, respectively. The experimental results, $(\beta'_{\text{TM}_0} - j\alpha'_{\text{TM}_0})/k_0 = 1.4966 - j0.00171$ on average, agree well with the calculated results. The loss is equivalent to 0.06 dB/μm or $L = 72$ μm. Unlike the cases of the TM modes in the MIM structure with $d_i = 730$ nm, in which the measured attenuations are about 13% smaller than the calculated values, the difference between the measured and the calculated attenuation is much less in this case. This can be ascribed to the angular distribution of the laser beam. In the calculation, the incident light is assumed to be a plane wave. However, the laser beam used in the measurement has a finite width and broadens a reflection resonance on the angular spectrum, and the broadening effect is stronger when the resonance is narrower. A quantified analysis of this broadening effect is discussed in Sec. V.

Figures 8(d) and 8(e) show N'_{TM_1} and $\alpha'_{\text{TM}_1}/k_0$ as functions of P_c. The experimental results, $(\beta'_{\text{TM}_1} - j\alpha'_{\text{TM}_1})/k_0 = 1.4273 - j0.00266$ on average, agree well with the calculated result. The loss is equivalent to 0.094 dB/μm or $L = 46$ μm. Similar to the cases of the TM modes in the MIM structure with $d_i = 730$ nm, the measured loss is about 14% smaller than the calculated result. Moreover, Figs. 8(f) and 8(g) show N'_{TM_2} and $\alpha'_{\text{TM}_1}/k_0$ as functions of P_c, and the experimental results, $(\beta'_{\text{TM}_2} - j\alpha'_{\text{TM}_2})/k_0 = 1.0949 - j0.0039$ on average, agree with the calculated result. The loss is equivalent to 0.14 dB/μm or $L = 32$ μm. The larger-than-expected measured loss is likely to be a result of the scattering loss caused by the rough Au/SiO$_2$ interfaces.

The measured TE reflectance angular spectra for the same structure is shown in Fig. 9(a). The TE resonances are weaker than the the TM resonances [Fig. 8(a)], because the portion of penetrated field into the absorptive Au claddings is less in the former. Figure 9(b) shows N'_{TE_0} as a function of P_c, and the average of the measurements yields $N'_{\text{TE}_0} = 1.3774$, with
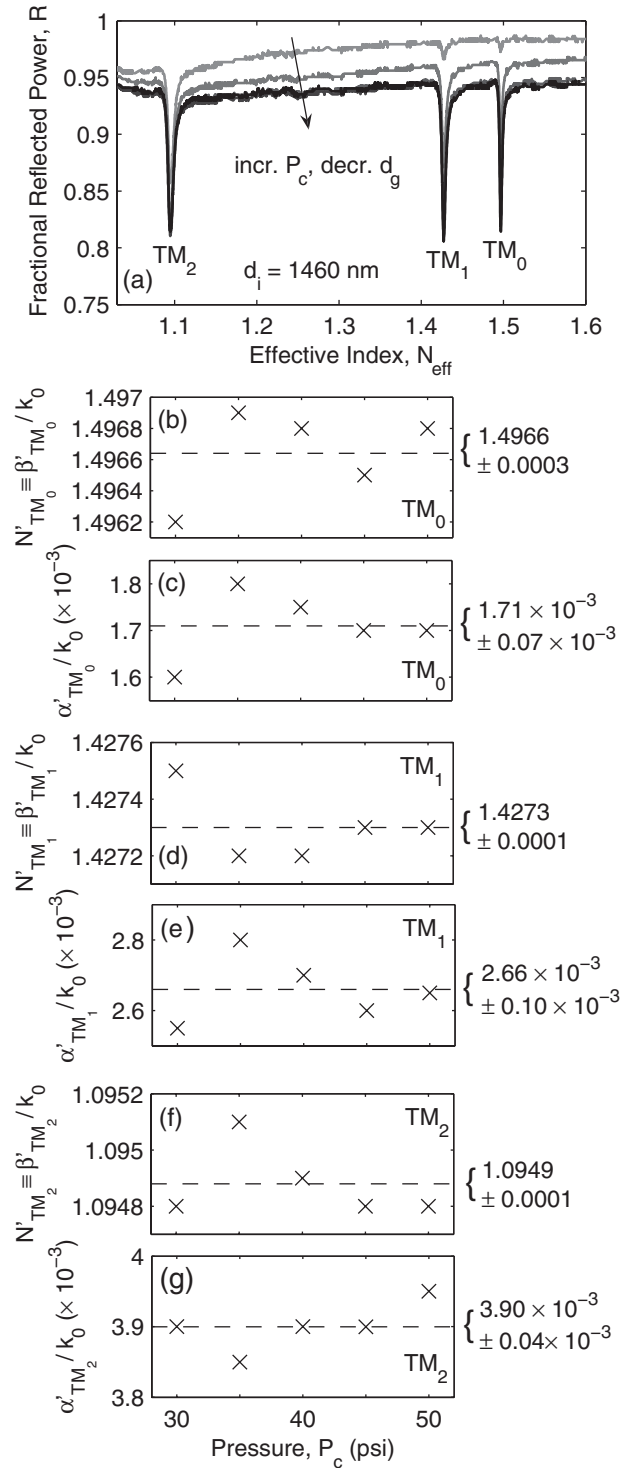

FIG. 8. (a) TM reflectance angular spectra for the structure in Fig. 5 with $d_i = 1460$ nm measured at various P_c. (b) N'_{TM_0} and (c) $\alpha'_{\text{TM}_0}/k_0$ of the TM$_0$ resonances. (d) N'_{TM_1} and (e) $\alpha'_{\text{TM}_1}/k_0$ of the TM$_1$ resonances. (f) N'_{TM_2} and (e) $\alpha'_{\text{TM}_2}/k_0$ of the TM$_2$ resonances.

a negligible standard deviation. Figure 9(c) shows $\alpha'_{\text{TE}_0}/k_0$ as a function of P_c, and the average of the measurements yields $\alpha'_{\text{TE}_0}/k_0 = 0.00071$, with a standard deviation $\sigma_\alpha = 0.00003$. The measured N'_{TE_0} and $\alpha'_{\text{TE}_0}/k_0$ are very self-consistent as P_c varies and agree well with the calculated result. The measured loss is much higher than the calculation because of the angular
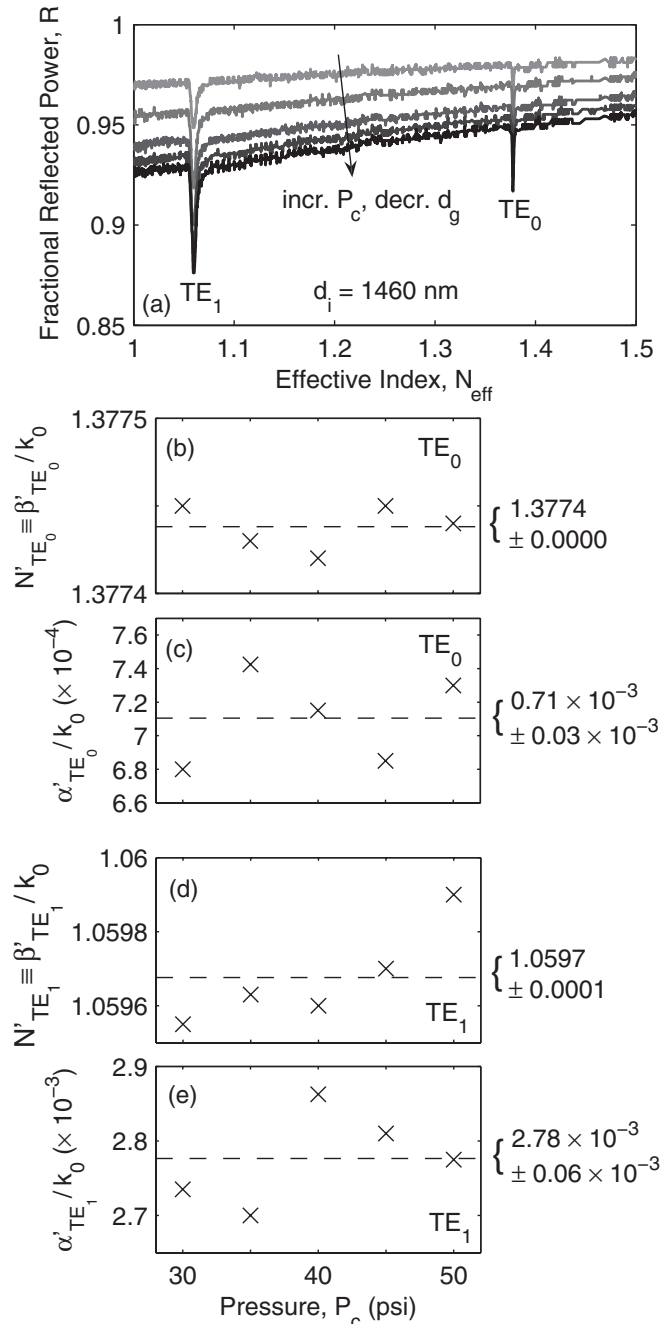
FIG. 9. (a) TE reflectance angular spectra for the structure in Fig. 5 with $d_i = 1460$ nm measured at various P_c values. (b) N'_{TE_0} and (c) α'_{TE_0}/k_0 of the TE$_0$ resonances. (d) N'_{TE_1} and (e) α'_{TE_1}/k_0 of the TE$_1$ resonances.

distribution of the incident laser beam. This effect is discussed in Sec. V.

Figures 9(d) and 9(e) show N'_{TE_1} and α'_{TE_1}/k_0 as functions of P_c. The experimental results, $(\beta'_{TE_1} - j\alpha'_{TE_1})/k_0 = 1.0597 - j0.00278$ on average, agree with the calculated result. The higher measured loss is contributed by both the angular distribution of the incident laser beam and the scattering loss.

In this section, all the modes in the two multimode MIM (Au-SiO$_2$-Au) structures have been experimentally measured and analyzed, and the measurement results agree well with the

calculation. It is also shown that, as mentioned in Sec. II, the fundamental TM$_0$ mode does not necessarily have the lowest attenuation. For example, in the 1460-nm core structure, the TE$_0$ mode has a lower attenuation, and all the other modes have comparable attenuation coefficients. Therefore, for the design and application of a large-core, multimode MIM waveguide like this, it is important to consider the effects of the other modes with lower or comparable attenuations in signal transmission.

V. DISCUSSION

As mentioned in Sec. IV, the angular spread of the laser beam broadens the measured reflection resonance on the angular spectrum. The resultant resonance is a convolution of the reflection resonance at plane-wave incidence and the angular distribution of the incident laser beam. The reflection resonance at plane-wave incidence can be calculated given the structure parameters of the the MIM, and the reflection resonance at experimental laser beam incidence can be calculated by the convolution of the former resonance and the angular profile of the incident laser beam. The laser beam used in this work has a FWHM of ∼0.12° in angle.[27] In Table II, the columns labeled "Calculated" correspond to the calculation results using $\tilde{n}_{Au} = 0.526 - j10.74$.[11] However, according to measurements in Refs. 6 and 13 and the results from Sec. IV, the absorption loss of Au is overestimated by about 15%. The reason for this overestimation is likely due to the sensitivity of the reflection/transmission measurements[11] to surface-roughness-induced scattering loss, which is mistakenly (and probably inevitably) included as the overall absorption loss. As a result, the column labeled "Adjusted calculated" represents 85% of the calculated loss. The columns labeled "Experimental" correspond to the unadjusted experimental results from Sec. IV. Given the measured reflection angular spectrum ("Experimental" column) and the profile of the incident laser beam, the absorption loss of Au can be adjusted until the width of the calculated resonance (i.e., convolution of the resonance at plane-wave incidence and the measured incident laser beam angular profile) agrees with the measured resonance width.
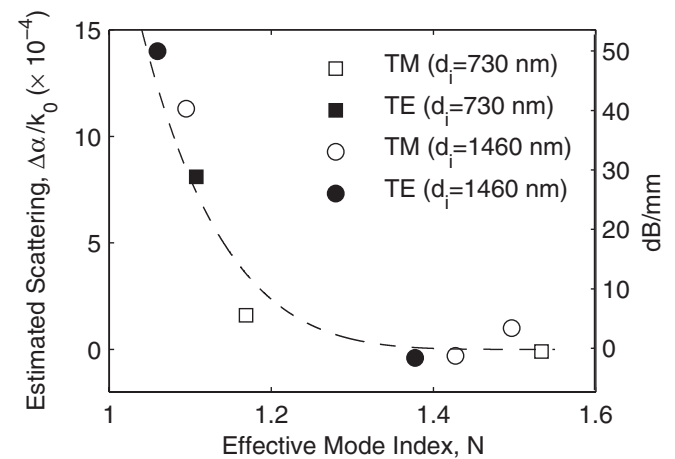

FIG. 10. Estimated scattering attenuations for the TM and TE modes based on the $\Delta\alpha/k_0$ column in Table II. The general trend is shown by the dashed curve.

TABLE II. Normalized propagation constants and attenuation coefficients obtained from calculations and measurements. The calculations are performed for unperturbed MIM structures, i.e., without the presence of a prism. The prime denotes original experimental results, and the double prime denotes adjusted experimental results by considering the angular distribution of the incident laser beam.

Structure	Mode	β/k_0 Calculated	β'/k_0 Experimental	α/k_0 Calculated	$0.85\alpha/k_0$ Adjusted calculated	α'/k_0 Experimental	α''/k_0 Adjusted experimental	$\Delta\alpha/k_0$ $(\alpha''-0.85\alpha)/k_0$
	TM_0	1.5392	1.5333	0.00281	0.00239	0.00247	0.00238	~ 0
$d_i = 730$ nm	TM_1	1.1764	1.1687	0.00668	0.00568	0.00588	0.00584	~ 0.0002
	TE_0	1.1020	1.1073	0.00256	0.00218	0.00310	0.00299	0.0008
	TM_0	1.4964	1.4966	0.00172	0.00146	0.00171	0.00156	~ 0.0001
	TM_1	1.4240	1.4273	0.00305	0.00259	0.00266	0.00256	~ 0
$d_i = 1460$ nm	TM_2	1.0801	1.0949	0.00320	0.00272	0.00390	0.00385	0.0011
	TE_0	1.3748	1.3774	0.00028	0.00024	0.00071	0.00020	~ 0
	TE_1	1.0464	1.0597	0.00148	0.00126	0.00278	0.00266	0.0014

The resonance widths adjusted by considering the broadening effect caused by the angular distribution of the incident laser beam are labeled "Adjusted experimental." The broadening is more significant for narrower resonances. The $\Delta\alpha/k_0$ column is defined as the difference between the adjusted experimental and adjusted calculated results, i.e., $\Delta\alpha \equiv \alpha'' - 0.85\alpha$. All the numbers in this column should be very close to zero if the absorption loss in Au claddings is the only source of loss.

However, $\Delta\alpha/k_0$ is nonzero for the modes with lower effective mode indices. The most probable reason for this discrepancy is scattering loss. Figure 10 shows the estimated scattering attenuation $\Delta\alpha/k_0$ for the TM and TE modes listed in Table II. The value of $\Delta\alpha/k_0$ increases rapidly as the effective mode index N decreases, which agrees qualitatively with the results shown in Ref. 10. The general trend is shown by the dashed curve in Fig. 10. The high scattering loss (up to 50 dB/mm) in the present work can be ascribed to the high surface and/or interface roughness for vacuum-deposited Au. A more detailed investigation of the scattering loss requires more measurement data from various samples and a straightforward and accurate model for the scattering loss in waveguide structures.

VI. SUMMARY AND CONCLUSIONS

The propagation constants and attenuation coefficients of all the TM and TE modes in multimode MIM waveguide structures have been investigated both theoretically and experimentally. The experiments are performed by using an ATR configuration, and the measurement results agree well with the calculation. It is also shown that the absorption loss for bulk Au in the literature[11] is overestimated by $\sim 15\%$. This overestimation is likely due to the inclusion of scattering loss at the Au surface as the overall Au absorption loss. In determining the overall waveguide mode propagation loss, these two loss mechanisms should be considered separately. According to the results from Table II, the Au absorption loss is dominant when high-N modes and scattering loss is relatively negligible. On the other hand, the absorption loss cannot explain the higher-than-expected loss in the low-N modes. The most probable explanation for the discrepancy is scattering loss, which is much larger for modes propagating at smaller zigzag angles.[12] On the other hand, although the theoretical analysis and experimental characterization are demonstrated on multimode MIM waveguides, similar analysis and measurements may be applied to other plasmonic waveguide structures, such as metal-slot waveguides[28–30] and hybrid plasmonic waveguides.[31–33]

In summary, in contrast to conventional dielectric optical waveguides, the higher-order modes in MIM structures may have lower loss than the fundamental mode, TM_0. Due to the typically high propagation attenuation of plasmonic mode, this property makes it possible to transmit waves at lower-loss modes, such as nonplasmonic, higher-order TM modes or TE modes, for applications that demand lower loss and fewer footprint constraints in an SP-based optical device or system.

*tgaylord@ece.gatech.edu

[1]H. Raether, *Surface Plasmons on Smooth and Rough Surfaces and on Gratings* (Springer-Verlag, 1988).

[2]W. L. Barnes, A. Dereux, and T. W. Ebbesen, Nature (London) **424**, 824 (2003).

[3]E. Ozbay, Science **311**, 189 (2006).

[4]E. Feigenbaum and M. Orenstein, J. Lightwave Technol. **25**, 2547 (2007).

[5]T. Goto, Y. Katagiri, H. Fukuda, H. Shinojima, Y. Nakano, I. Kobayashi, and Y. Mitsuoka, Appl. Phys. Lett. **84**, 852 (2004).

[6]J. A. Dionne, H. J. Lezec, and H. A. Atwater, Nano Lett. **6**, 1928 (2006).

[7]S. I. Bozhevolnyi, V. S. Volkov, E. Devaux, and T. W. Ebbesen, Phys. Rev. Lett. **95**, 046802 (2005).

[8]E. Verhagen, J. A. Dionne, L. Kuipers, H. A. Atwater, and A. Polman, Nano Lett. **8**, 2925 (2008).

[9]E. N. Economou, Phys. Rev. **182**, 539 (1969).

[10]B. Prade, J. Y. Vinet, and A. Mysyrowicz, Phys. Rev. B **44**, 13556 (1991).

[11]P. B. Johnson and R. W. Christy, Phys. Rev. B **6**, 4370 (1972).

[12]P. K. Tien, Appl. Opt. **10**, 2395 (1971).

[13]C.-I. Lin and T. K. Gaylord, Appl. Opt. **48**, 3603 (2009).

[14]C.-I. Lin and T. K. Gaylord, Appl. Opt. **49**, 936 (2010).

[15]C.-I. Lin and T. K. Gaylord, Opt. Lett. **35**, 3814 (2010).

[16]E. Anemogiannis, E. N. Glytsis, and T. K. Gaylord, J. Lightwave Technol. **17**, 920 (1999).

[17]A. Otto, Zeitschrift Fur Physik **216**, 398 (1968).

[18]R. Ulrich, J. Opt. Soc. Am. **60**, 1337 (1970).

[19]P. K. Tien and R. Ulrich, J. Opt. Soc. Am. **60**, 1325 (1970).

[20]A. E. Craig, G. A. Olson, and D. Sarid, Opt. Lett. **8**, 380 (1983).

[21]J. C. Quail, J. G. Rako, and H. J. Simon, Opt. Lett. **8**, 377 (1983).

[22]F. Z. Yang, G. W. Bradberry, and J. R. Sambles, Phys. Rev. Lett. **66**, 2030 (1991).

[23]Metricon Corporation, http://www.metricon.com/.

[24]E. Anemogiannis and E. N. Glytsis, J. Lightwave Technol. **10**, 1344 (1992).

[25]A. C. Adams, F. B. Alexander, C. D. Capio, and T. E. Smith, J. Electrochem. Soc. **128**, 1545 (1981).

[26]S. Matsuo and M. Kiuchi, Jpn. J. Appl. Phys., Part 2 **22**, L210 (1983).

[27]C.-I. Lin, Ph.D. thesis, Georgia Institute of Technology, 2011.

[28]G. Veronis and S. Fan, J. Lightwave Technol. **25**, 2511 (2007).

[29]L. Liu, Z. Han, and S. He, Opt. Express **13**, 6645 (2005).

[30]F. Kusunoki, T. Yotsuya, J. Takahara, and T. Kobayashi, Appl. Phys. Lett. **86**, 211101 (2005).

[31]R. F. Oulton, V. J. Sorger, D. A. Genov, D. F. P. Pile, and X. Zhang, Nat. Photonics **2**, 496 (2008).

[32]D. Dai and S. He, Opt. Express **17**, 16646 (2009).

[33]H.-S. Chu, E.-P. Li, P. Bai, and R. Hegde, Appl. Phys. Lett. **96**, 221103 (2010).